

# Mechanical Properties of 3D-Printed Polymeric Cellular Structures Based on Bifurcating Triply Periodic Minimal Surfaces

Yanhong Zhang, Junming Zhang, Xiaotian Chen, Weidong Yang, Hao Chen,\*  
 Shunai Che,\* and Lu Han\*

**Triply periodic minimal surface (TPMS) structures hold great potential as mechanical materials due to their exceptional strength-to-weight ratios and energy absorption capabilities. However, the limited number of known structural types poses a barrier to a profound comprehension and utilization of their mechanical properties. Herein, the mechanical properties and deformation mechanisms of eight recently discovered bifurcating TPMS structures characterized by noncubic symmetries are reported. These polymeric metamaterials are fabricated by fused deposition modeling, followed by quasistatic compression tests conducted across multiple loading directions to evaluate their anisotropic mechanical responses. Experimental results show that the bifurcating TPMS structures generally exhibit enhanced strength compared to classical counterparts, particularly in the direction of bifurcating deformation. Additionally, finite-element simulation is employed to simulate the failure behavior and it is found that stress concentration varies in different structures, which is closely related to the geometry types and deformation mechanisms. These results demonstrate the suitability of bifurcating TPMS structures for load-bearing applications and may pave the way for innovative designs and fabrication of efficient lightweight mechanical structures in the future.**

considerable interest in developing novel functional materials by drawing inspiration from nature's designs.<sup>[2]</sup> Compared to lattice structures that have been extensively investigated,<sup>[3]</sup> the unique topological features of TPMSs make them highly desirable for multifunctional applications, which has motivated researchers to exploring their mechanical and structural properties in depth.<sup>[4]</sup> Particularly, TPMSs feature smooth surfaces devoid of sharp edges and corners, thereby effectively avoiding stress concentrations and enhancing load-bearing capacity and stability, exhibiting high stiffness-to-weight ratio, large surface-to-volume ratio, and enhanced mechanical energy absorption capabilities.<sup>[5]</sup> These advantageous properties render TPMSs highly valuable across multiple aspects of engineering and offer broad application potential in lightweight structures, energy storage and conversion, thermal management, wave propagation control, healthcare applications, etc.<sup>[6]</sup>

Up to now, several experimental, computational, and analytical methods have been developed to investigate the linear and nonlinear mechanical responses of TPMS structures, including elastic properties, yield strength, energy absorption, and deformation mechanisms.<sup>[7]</sup> The mechanical behaviors of TPMSs are affected by a multitude of factors, including printing substrates, topological configurations, relative densities, repeating units, lattice orientations, etc.<sup>[8]</sup> In particular, when the substrate is fixed, the mechanical properties of structures are determined by

## 1. Introduction

TPMS represents a nonintersecting, infinite 3D periodically organized continuous surface with vanished mean curvature, dividing space into two intricately intertwined subdomains while preserving open cavities.<sup>[1]</sup> TPMSs have been extensively identified across various biological systems, and their highly symmetrical structures coupled with optimized physical properties have sparked

Y. Zhang, X. Chen, L. Han  
 School of Chemical Science and Engineering  
 Tongji University  
 1239 Siping Road, Shanghai 200092, P. R. China  
 E-mail: luhan@tongji.edu.cn

J. Zhang, W. Yang  
 School of Aerospace Engineering and Applied Mechanics  
 Tongji University  
 100 Zhangwu Road, Shanghai 200092, P. R. China

The ORCID identification number(s) for the author(s) of this article can be found under <https://doi.org/10.1002/adem.202402507>.

DOI: 10.1002/adem.202402507

H. Chen  
 Institute of Mathematical Sciences  
 ShanghaiTech University  
 393 Middle Huaxia Road, Shanghai 201210, China  
 E-mail: chenhao5@shanghaitech.edu.cn

S. Che  
 School of Chemistry and Chemical Engineering  
 Frontiers Science Center for Transformative Molecules  
 State Key Laboratory of Metal Matrix Composites  
 Shanghai Key Laboratory for Molecular Engineering of Chiral Drugs  
 Shanghai Jiao Tong University  
 800 Dongchuan Road, Shanghai 200240, China  
 E-mail: chesa@sjtu.edu.cn

their geometric characteristics. Consequently, multifunctional TPMS materials with controllable geometric morphology and mechanical properties can be realized by geometric design strategies such as interpenetrative,<sup>[9]</sup> hybrid,<sup>[10]</sup> gradient,<sup>[11]</sup> heterogeneous,<sup>[12]</sup> multiscale,<sup>[13]</sup> and topology optimization.<sup>[14]</sup> However, current advancements are primarily based on the most symmetric and topologically simplest TPMSs with genus 3. These include well-known primitive (P), diamond (D), and gyroid (G) surface structures with cubic symmetry. The focus of research on these highly symmetrical structures significantly restricts the exploration of new intrinsic structural designs and mechanical properties for TPMS-based materials.

Hermann Schwarz, the German mathematician who constructed the first TPMSs including P and D, was already aware of their tetrahedral and rhombohedral deformations, now known as tP, tD, rPD, etc. Tetrahedral and rhombohedral deformations of the G surface were numerically discovered in the 1990 s and recently proved by one of the authors.<sup>[15]</sup> Recently, new orthorhombic deformations of the D and hexagonal (H) surfaces have been mathematically constructed. The noncubic deformations of TPMS would result in continuous variations of structural configurations, offering an infinite variety of mechanical characteristics. As the underlying lattice deforms, a TPMS typically responds by undergoing a unique deformation while maintaining its minimal surface characteristics. However, in certain special cases, the same lattice deformation can lead to distinct mathematical solutions for the TPMS at specific points—a phenomenon known as bifurcation. In such instances, the structure splits into different configurations, resulting in varied deformations. These bifurcating structures merit particular attention due to their unique mathematical and physical properties. Recently, eight bifurcating TPMSs among classical TPMS families were first predicted using the Morse index and later explicitly confirmed by Chen while discovering new examples of TPMSs.<sup>[15,16]</sup> However, the mechanical properties of these bifurcating TPMS structures have never been reported, and it remains unknown whether their bifurcated feature brings unique mechanical properties.

In this study, the mechanical properties and deformation mechanisms of the eight bifurcating TPMS structures have been investigated. All structural models were fabricated using fused deposition modeling (FDM) 3D printing. These structures are particularly interesting due to their deformation modes and noncubic symmetry. Therefore, compression tests were performed in multiple orientations and compared with the three most common TPMS structures, namely, the G, D, and P surfaces. Additionally, finite-element (FE) simulations were conducted to analyze the stress distribution and transfer during compression deformation to provide a deeper understanding of the structural compressive mechanical behavior.

## 2. Results and Discussion

### 2.1. Construction of the Bifurcating TPMS Structures

Every TPMS of genus 3 admits a Weierstrass representation of the form<sup>[17]</sup>

$$z \mapsto \int^p (1 - z^2, i(1 + z^2), 2z) \frac{dz}{w} \quad (1)$$

where  $w^2$  is a polynomial of degree 8 or 7.

The rPD surfaces (Figure 1a) can be seen as consisting of catenoids bounded by antiparallel triangles. Its Weierstrass representation is given by  $w^2 = z(z^3 - a^3)(z^3 + a^{-3})$ . Let  $r$  be the inradius of the triangles and  $h$  be the height of the catenoids. It was found that the ratio  $h/r$  attains maximum at  $a \approx 0.494722$ ,<sup>[16a]</sup> corresponding to our rPD-max surface.

The H surfaces (Figure 1b) can also be seen as consisting of triangular catenoids, but bounded by parallel triangles. Its Weierstrass representation is  $w^2 = z(z^3 - a^3)(z^3 - a^{-3})$ . Again, let  $r$  be the inradius of the triangles and  $h$  be the height of the catenoids. It was found that the ratio  $h/r$  attains maximum at  $a \approx 0.49701$ ,<sup>[16a]</sup> corresponding to our H-max surface.

Similarly, the tP surfaces (Figure 1c) can be seen as consisting of square catenoids with Weierstrass representation of  $w^2 = z^8 + az^4 + 1$ . Let  $b$  be the edge length of the squares and  $h$  be the height of the catenoids. The ratio  $h/b$  attains maximum at  $a \approx 28.7783$ ,<sup>[16a]</sup> corresponding to our tP-max surface.

From the tP surface with  $a \approx 7.40284$ , a new deformation family named tΠ was recently noticed.<sup>[16b]</sup> They share the same tetragonal lattices with the tP surfaces, but with different symmetry. As one deforms the tetragonal lattice, the horizontal handles deform uniformly along the tP deformation path. But along the tΠ deformation path, the handles in the  $x$  direction shrink while the handles in the  $y$  direction expand. The tΠ family turns out to be a subfamily of oPa, a 2-parameter orthorhombic deformation family of Schwarz P surface, which is in turn a subfamily of Meeks family.

The tD surfaces are conjugate of tP surfaces, so their Weierstrass data was given by  $w^2 = -z^8 - az^4 - 1$ . From the tD surface with  $a \approx 7.40284$ , a new deformation family named tΔ was recently discovered.<sup>[16b]</sup> They share the same tetragonal lattices with the tD surfaces, but with different symmetry. To construct a t-Delta surface (Figure 1d), one considers a tetragonal box and a minimal hexagon with free boundary condition on the lateral faces of the box and fixed boundary condition along middle lines in the top and bottom faces. Then the reflections in the lateral faces and order-2 rotations around the fixed boundaries give a TPMS of genus 3. The tD surfaces correspond to one solution of this boundary value problem, characterized by an order-2 rotation axis in the middle of the box. This is actually the only solution when the box is sufficiently high. But for small heights, another solution was recently noticed, corresponding to the new tΔ surface.

From the H surface with  $a \approx 0.71479$ , a new deformation family that shares the same hexagonal lattices as the H surfaces was discovered.<sup>[16c]</sup> The H family and the new family are both subfamilies in the orthorhombic oH family. To construct an oH surface (Figure 1e), one considers an orthorhombic box, and a minimal octagon with free boundary conditions on the lateral faces of the box, and fixed boundary conditions along middle lines in the top and bottom faces, with an inversion center. Then the reflections in the lateral faces and order-2 rotations around the fixed boundaries give a TPMS of genus 3. The oPb surfaces give one solution, characterized by an order-2 rotation axis in the middle. The oH surfaces give another solution.

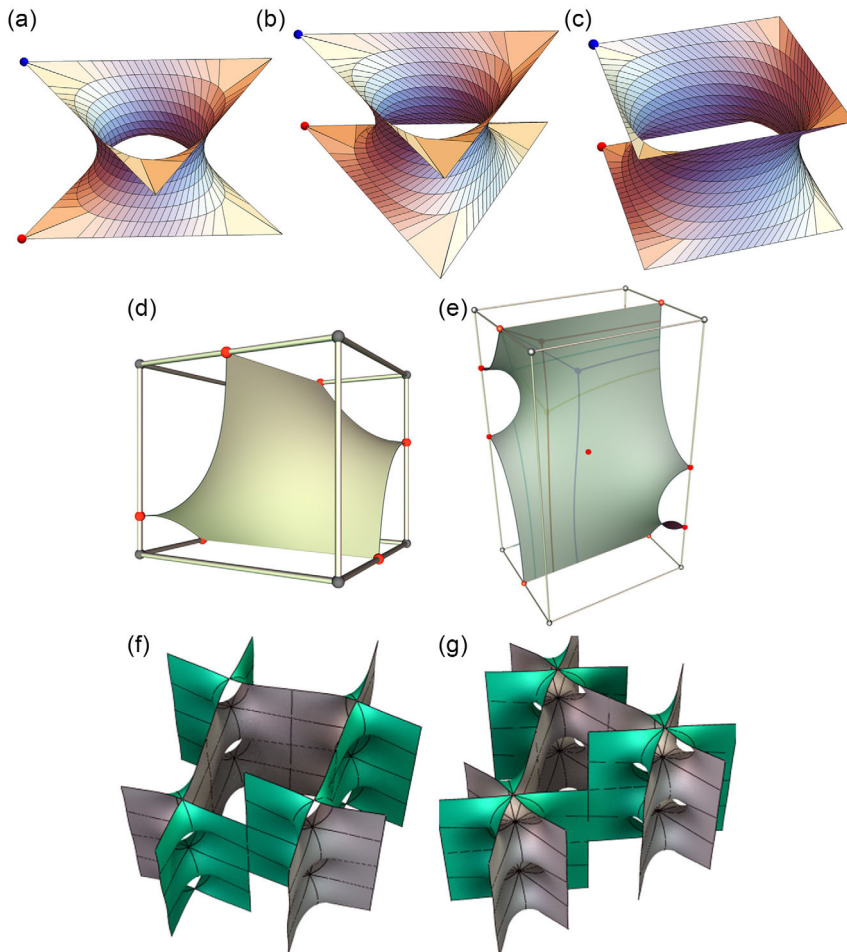


**Figure 1.** Illustration of the mathematical models. a) rPD surface, b) H surface, c) tP surface, d) oDelta, a surface in the orthorhombic family, which includes tDelta surfaces as a special case, e) oH, a surface in the orthorhombic family, f) tG, and g) rGL surface. (a–c) Reproduced with permission.<sup>[15]</sup> Copyright 2021, Indiana Univ. Math. J. (d) Reproduced with permission.<sup>[16b]</sup> Copyright 2021, American Mathematical Society; (e) Reproduced with permission.<sup>[16c]</sup> Copyright 2021, American Mathematical Society; (f–g) Reproduced with permission.<sup>[24]</sup> Copyright 2024, Walter de Gruyter GmbH, Berlin/Boston.

From the tD surface with  $a \approx 28.7783$ , conjugate to the tP-max surface, emerges a tetragonal deformation family tG containing the G surface (Figure 1f). It shares the same lattice as the tD surfaces, but with different symmetry. The tG surfaces were first discovered by Fogden et al.<sup>[18]</sup> and recently rigorously proved.<sup>[15]</sup> They only exist for tetragonal lattices with sufficiently small heights. As one decreases the height from the bifurcation point, the surface could deform along the rPD path and preserve the straight lines parallel to the order-4 rotation axis, or deform along the rGL path while these straight lines deform into a helices, and the order-4 rotation symmetries become screw symmetries.

From the rPD surface with  $a \approx 2.02133$ , conjugate to the rPD-max surface, emerges a rhombohedral deformation family rGL (Figure 1g), containing the G surface and the Lidinoid. It shares the same lattice as the rPD surfaces, but with different symmetry. The rGL surfaces were also discovered by Fogden et al.<sup>[18]</sup> and recently rigorously proved.<sup>[15]</sup> They only exist for rhombohedral lattices with sufficiently small heights. As one decreases the height from the bifurcation point, the surface could deform along the rPD

path and preserve the straight lines parallel to the order-3 rotational axis, or deform along the rGL path while these straight lines deform into a helices, and the order-3 rotation symmetries become screw symmetries. The relevant structures are shown in Figure 1.

The structural units of eight bifurcating TPMSs were obtained using Surface Evolver. For surfaces in the tD family (i.e., tD-tG and tD-tDelta surfaces), we generated their “flächenstück” bounded by six straight edges by minimizing the surface area. Other surfaces lie in the tP, rPD, and H families; we generated the corresponding square or triangle catenoids by minimizing either the surface area or the Willmore energy (integral of squared mean curvature). The results were then imported into the 3D modeling software Houdini to get the periodic lattices, and then Boolean operations were performed with a cube to obtain the target structure model. Considering their structural anisotropy, which causes mechanical properties to vary with direction, the structures were oriented along different axes to enable corresponding printing directions. The modeling process and the loading direction of the structures are shown in Figure 2

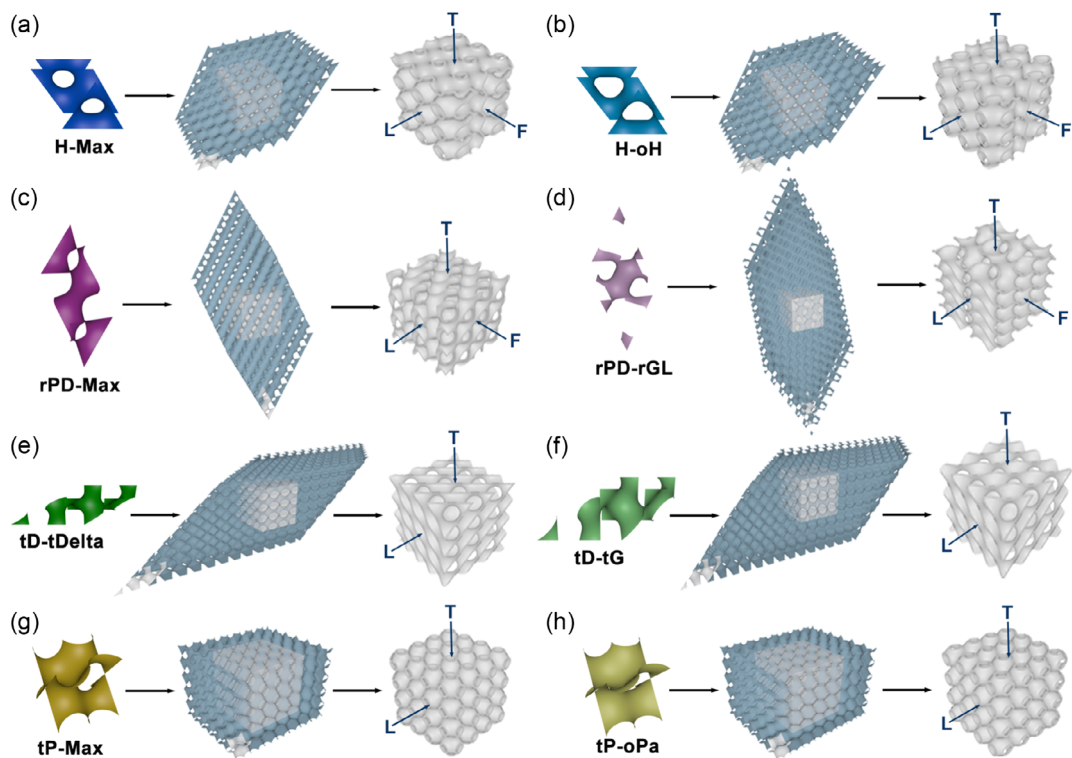


**Figure 2.** Schematic diagram of the modeling process and loading direction of eight bifurcating TPMS structures. a) H-Max, b) H-oH, c) rPD-Max, d) rPD-rGL, e) tD-tDelta, f) tD-tG, g) tP-Max, and h) tP-oPa.

with the representative measuring directions from top (-T), left (-L), and front (-F), respectively. Some models are symmetrical equivalent in left and front directions, so only one direction was studied. The physical models were obtained by FDM 3D printing with polylactic acid (PLA) filament. The size of all printed models is  $40 \times 40 \times 40$  mm (Figure 3).

## 2.2. Mechanical Characterizations

To investigate the mechanical properties of the eight bifurcating types of TPMS structures, uniaxial quasistatic compression tests were carried out using an FR-103C testing machine with 50 KN load cell. The experiments were performed at room temperature with a strain rate of  $1 \text{ mm min}^{-1}$ . The loading direction was consistent with the printing direction of all samples, and the test was terminated upon reaching the densification stage. As shown in Figure 4, all mechanical curves exhibited three distinct regions: the linear elastic stage, the plastic stage, and the densification stage. In the linear elastic stage, the slope of the stress-strain curve corresponds to the elastic modulus of the structure. The plastic stage was characterized by stress fluctuation or a yield plateau, which are indicative of the deformation mechanism of the structure. Finally, the densification stage shows a sharp increase in stress with increasing strain.

For H-Max (Figure 4a), the mechanical properties exhibited notable variations across the three directions. Specifically, the peak stress values for H-Max-L and H-Max-F were  $\approx 80\%$  higher than those of H-Max-T, while the elastic modulus exceeded that

of H-Max-T by 115%. In the plastic stage, H-Max-F showed a relatively stable deformation process, while H-Max-T and H-Max-L exhibited significant fluctuations, suggesting multiple instances of collapsing and reloading during compression. On the contrary, H-oH exhibited smaller mechanic anisotropy (Figure 4b). The linear elastic stages for all three directions were almost identical, with the peak stress variations within 3%. However, the plastic deformation behavior of H-oH was similar to that of H-Max, with successive increase in deformation fluctuations observed for H-oH-F, H-oH-T, and H-oH-L. The comparison of the mechanical properties of the two structures showed that difference in bifurcation deformation has a notable influence on the structure's mechanical anisotropy.

rPD-Max exhibited obvious mechanical anisotropy (Figure 4c), with distinct stress-strain curves in the linear elastic stage across different directions. Notably, the plastic deformation behavior of rPD-Max-L showed repeated collapse and reloading, judging from the severe alternation of peaks and valleys. The structures in the other two directions showed relatively mild plastic deformation. For rPD-rGL (Figure 4d), the stress-strain curves of rPD-rGL-L and rPD-rGL-F were similar, aside from differences in plastic stage fluctuations. Although rPD-rGL-T exhibited the lowest stress-strain curve, its plastic behavior was close to ideal plastic deformation, demonstrating more stable energy absorption characteristics.

For tD-tDelta, tD-tG, tP-Max, and tP-oPa, the front and lateral directions are symmetrical equivalent, so only one of them was tested. The tD-tDelta-T showed lower peak stress but exhibited

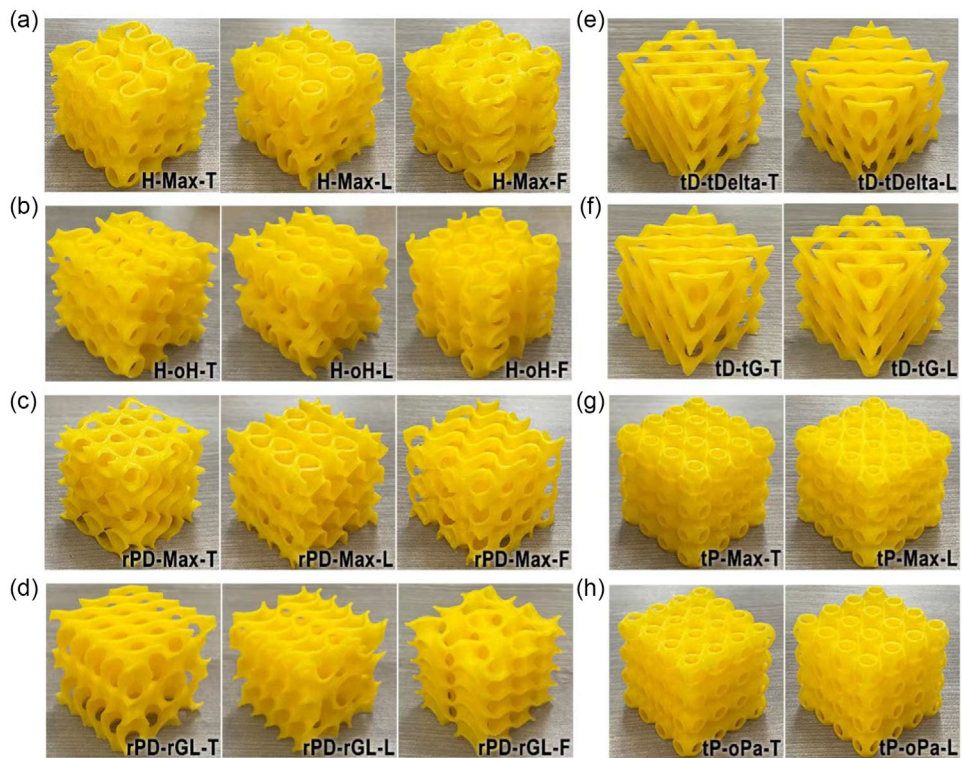


**Figure 3.** Optical photos of 3D-printed bifurcating TPMS structures with different orientations. a) H-Max, b) H-oH, c) rPD-Max, d) rPD-rGL, e) tD-tDelta, f) tD-tG, g) tP-Max, and h) tP-oPa.

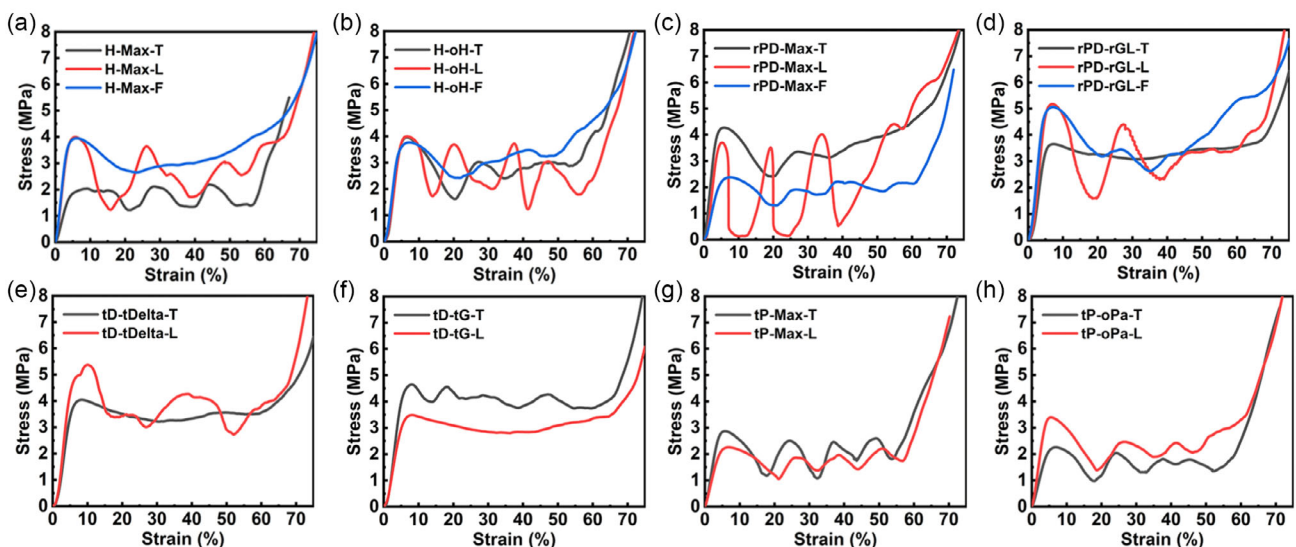


**Figure 4.** Stress–strain curves of bifurcating TPMS structures with different directions. a) H-Max, b) H-oH, c) rPD-Max, d) rPD-rGL, e) tD-tDelta, f) tD-tG, g) tP-Max, and h) tP-oPa.

stable plastic deformation. In contrast, higher peak stress with unstable plastic deformation was observed for tD-tDelta-L (Figure 4e). The mechanical behavior of tD-tG was similar to that of tD-tDelta; however, the lattice orientation inversely affected its mechanical properties, resulting in tD-tG-T being stronger (Figure 4f). Similarly, the difference in mechanical curves

between tP-Max and tP-oPa was also direction dependent. Plastic deformation across different directions was comparable, and the anisotropy was mainly reflected in peak stress and elastic modulus (Figure 4g,h).

To understand the deformation mechanisms of these structures, deformation snapshots were captured during compression

at different strain levels. **Figure 5** illustrates the deformation processes of H-Max and H-oH structures. The H-Max-T initially exhibited an oblique shear band (Figure 5a), followed by a layer-by-layer collapse mechanism. During this process, the voids gradually closed from the central position toward both ends. This phenomenon was consistent with the fluctuations observed in the plastic stage of the stress-strain curve. Similarly, the H-Max-L structure displayed a comparable layer-by-layer deformation pattern; however, the shear band orientation was nearly horizontal. In contrast, the H-Max-F demonstrated overall deformation characteristics during compression, with microcracks evenly distributed across the structure. This behavior aligned with the plain plastic stage in its stress-strain curve.

The compressive responses of the samples were further analyzed using FE methods. While different printing paths may affect thermal history in FDM, it was reported that these differences are mainly reflected in the material strength rather than modulus.<sup>[19]</sup> The elastic properties of the material vary little across different printing directions.<sup>[20]</sup> The stress distributions and stress concentrations in different structures are mainly determined by the geometric shape. Therefore, an isotropic material model was adopted for obtaining stress distribution, which greatly improves computational efficiency without significantly affecting the prediction of stress distribution. The stress distribution from the FE simulation, as depicted in Figure 5b, is closely linked to the deformation shear bands. Initially, the stress in H-Max-T was centralized and then spread across each layer, resulting in layered compaction until densification. Conversely, the stress in H-Max-L was initially concentrated at

the top and bottom, leading to the collapse of the upper structure. As strain increased, the stress migrated toward the central region, transforming the structure into a highly stressed solid. For H-Max-F, uniformly distributed vertical stress bands were observed, which shortened vertically and widened horizontally as strain increased until densification was achieved.

Since the structural units of H-OH and H-Max are similar, their deformation processes exhibited comparable characteristics. For H-OH structure (Figure 5c), all three axes showed layer-by-layer deformation. The H-OH-L was notably distinct, exhibiting horizontal shear bands alongside severe oscillations in the stress-strain curve. Both H-OH-T and H-OH-F structures developed oblique shear bands but differed in their compression patterns: H-OH-T from the middle to both ends, and H-OH-F from top to bottom. In the FE simulation (Figure 5d), the initial stress distribution of the H-OH-T structure was X-shaped, with concentrated stress and strain in the central part, which then transferred to both ends until densification. The H-OH-L and H-OH-F exhibited horizontal and vertical stress bands, respectively. Notably, both H-Max and H-OH structures are composed of basic unit of catenoids, where the waist is the weakest point. Therefore, both structures exhibited a similar deformation mechanism under compressive load, breaking from the waist.

The compression and FE simulations for the rPD-Max and rPD-rGL structures are presented in **Figure 6**. The deformation mode of rPD-Max showed directionality characteristics (Figure 6a). rPD-Max-T showed a stable overall compression behavior with widespread microcracks distributed uniformly. It is worth noting that the rPD-Max-T structure consists of

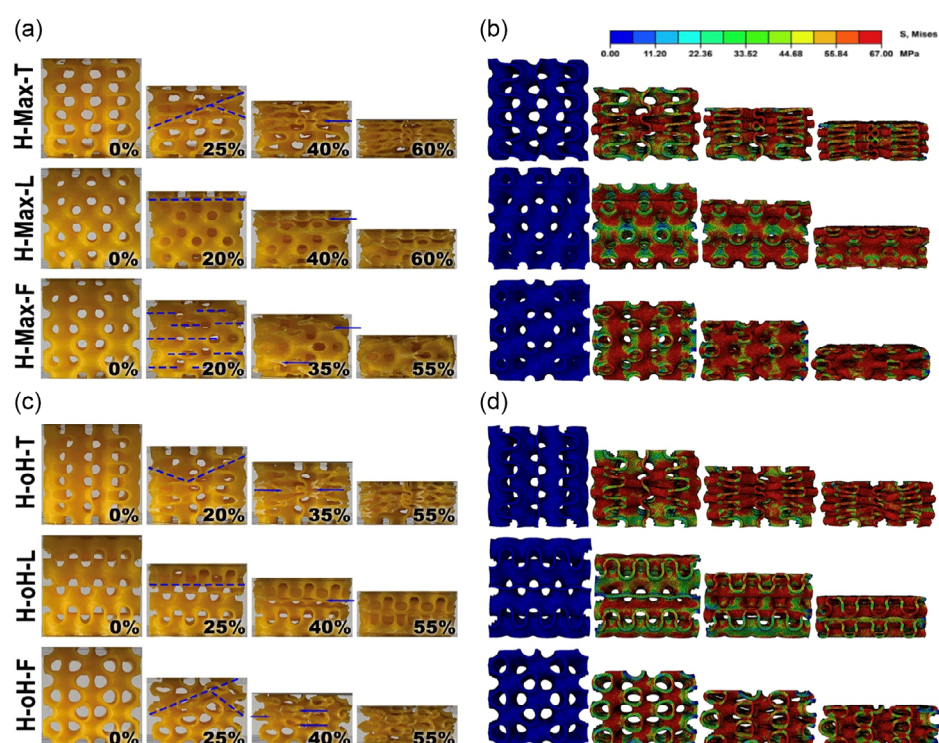


**Figure 5.** Compression processes and FE simulations of a,b) H-Max and c,d) H-OH structures under different load directions. The blue dotted lines represent shear bands, and the colors indicate the local level of stress (von Mises stress).

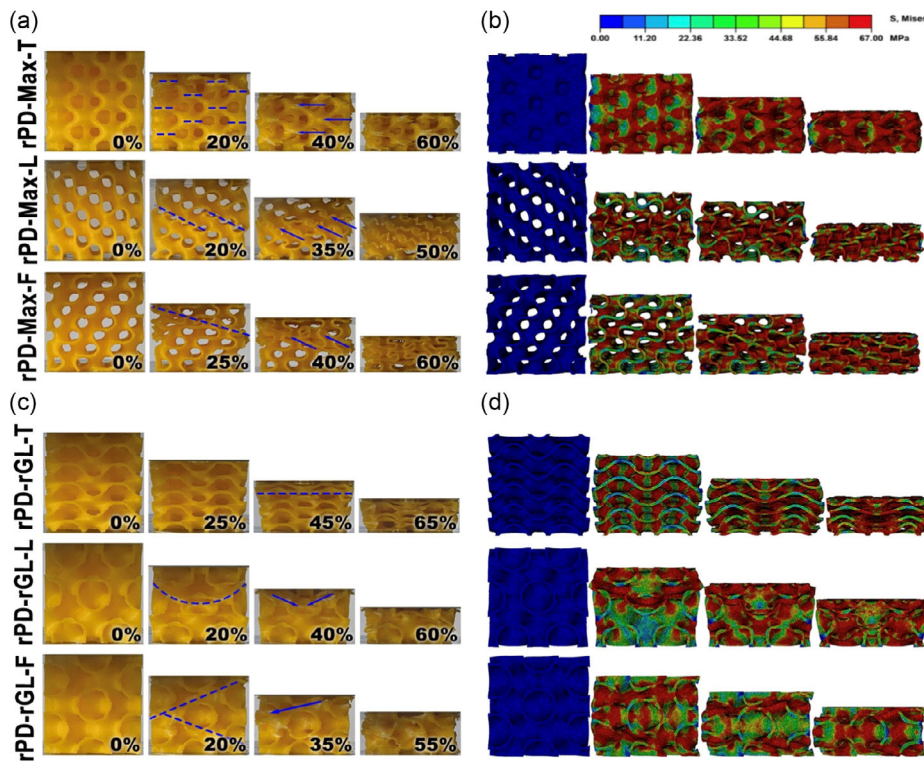


**Figure 6.** Compression process and FE simulations of a,b) rPD-Max and c,d) rPD-rGL structures under different load directions. The blue dotted lines represent shear bands, and the colors indicate the local level of stress (von Mises stress).

catenoid-based units. The waists of these catenoids are oriented perpendicularly to the loading direction, which resulted in horizontal cracking patterns during deformation. This led to the concurrent failure of all structural components and contributed to the observed stable compressive behavior, characterized by uniformly distributed microcracks. The rPD-Max-L structure experienced slip fractures propagated along the pore direction, forming oblique shear bands. This behavior is attributed to the weak structural connectivity across the pore region during slippage, causing a sharp drop in stress. As strain increased, rupture occurred within the pore regions successively, resulting in significant fluctuations in the stress-strain curve. The rPD-Max-F also developed an oblique shear band under load, with pores gradually closed from top to bottom. The FE analysis presented in Figure 6b reveals that the stress distribution within the rPD-Max-T structure was generally uniform. However, there were notable areas of localized stress non-uniformity. These localized stress variations led to different extents of localized failure. Despite these failures, the overall deformation behavior remained consistent throughout. Additionally, the high-stress distributions observed in both the rPD-Max-L and rPD-Max-F are consistent with the experimental shear bands.

The deformation behavior of rPD-rGL under the three loading directions exhibited different characteristics (Figure 6c). rPD-rGL-T was uniformly compressed under loading, maintaining equal distance between layers. rPD-rGL-L appeared as a cambered shear band and collapsed gradually from top to bottom. There are two opposite oblique shear bands displayed in rPD-rGL-F, with failure

along these shear bands. The stress distribution in rPD-rGL-T showed an overall uniform pattern, with localized stress concentrations. In contrast, the stress in rPD-rGL-L and rPD-rGL-F was concentrated along the experimental observed deformation shear zones (Figure 6d).

Figure 7 illustrates the compression deformation and FE simulations of tD-tDelta and tD-tG structures. For tD-tDelta, the difference between tD-tDelta-T and tD-tDelta-L lies in the number of repeating units along the loading direction, a characteristic also observed in tD-tG-T and tD-tG-L. As shown in Figure 7a, both the D-tDelta-T and tD-tDelta-L underwent a layer-by-layer deformation; however, the former was compressed from bottom to top, while the latter was compressed from top to bottom. The same was observed for tD-tG-T and tD-tG-L, but both were compressed from top to bottom (Figure 7c). When comparing the experimental results and simulations, they exhibit consistent layer-by-layer deformation mechanisms, as evidenced by the FE simulations (Figure 7b,d); however, the order in which layers collapse may differ. The discrepancies between simulation and experimental results may arise from three key factors: manufacturing errors inherent to the layer-by-layer process, which particularly affect weak connections in structures like tD-tG; differences in boundary conditions, as simulations assume uniform constraints while experiments have asymmetrical loading due to fixed lower ends and moving upper plates; and simplified friction coefficients in simulations that may overconstrain certain structures. Despite these local differences, the overall deformation mechanisms remain consistent between

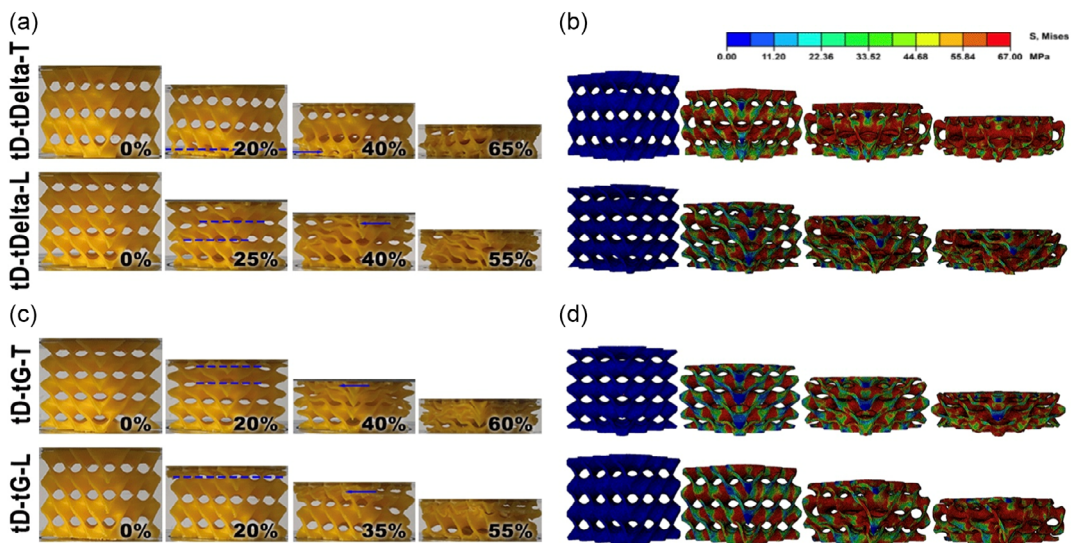


**Figure 7.** Compression process and FE simulations of a,b) tD-tDelta and c,d) tD-tG structures under different load directions. The blue dotted lines represent shear bands, and the colors indicate the local level of stress (von Mises stress).

simulations and experiments, with discrepancies decreasing as strain increases. In addition, from the comparison between the tD-tDelta and tD-tG structures, it was found that increased periodicity along the loading direction enhances compressive mechanical properties.

The compression behavior and FE simulations of the tP-Max and tP-oPa structures are shown in Figure 8. The tP-Max-T and tP-Max-L structures are different in the orientation of the long axis of their elliptical pores relative to the applied load, where the former is parallel to the loading direction while the latter is perpendicular to it. A similar distinction exists between

tP-oPa-T and tP-oPa-F, but in contrast to the situation with tP-Max-T and tP-Max-L. As shown in Figure 8a, a V-shaped shear band appeared in the tP-Max-T structure, causing progressive collapsed from top to bottom along the shear band. The tP-Max-L showed a horizontal shear band and failed layer by layer. For tP-oPa (Figure 8c), the tP-oPa-T structure failed via compression from both ends toward the center with horizontal shear bands, while the tP-oPa-F structure experienced gradually collapse along the X-shaped shear bands. The experimental observations were closely matched by the FE simulations, as evidenced by the observed cracks and simulated high-stress regions

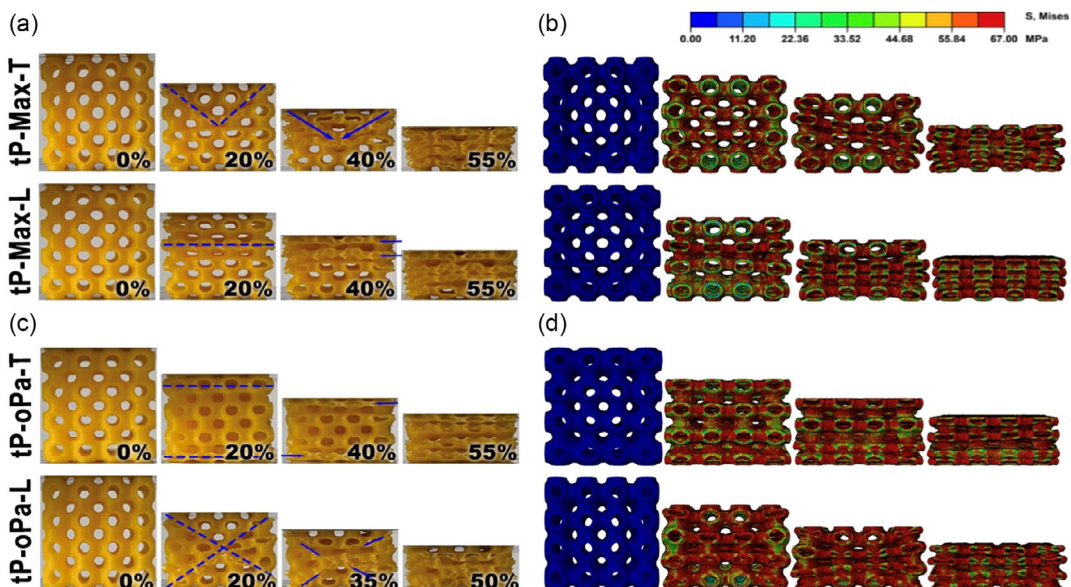


**Figure 8.** Compression process and FE simulations of a,b) tP-Max and c,d) tP-oPa structures under different load directions. The blue dotted lines represent shear bands, and the colors indicate the local level of stress (von Mises stress).

(Figure 8b,d). It was found that the mechanical properties were significantly affected by the orientation of the long axis of the elliptical pore relative to the applied load. When aligned parallel to the loading direction, the vertical ellipses induced tensile deformation patterns that enhanced structural integrity.

### 2.3. Discussion

To better understand the impact of bifurcation on the mechanical properties of TPMS structures, the mechanical properties of eight bifurcating TPMSs were compared with the three common TPMSs, namely, G, D, and P surface structures. The 3D-printed structures are shown in Figure 9a, with four typical crystallographic directions investigated. The stress–strain curves revealed that G, D, and P structures exhibited increased levels of mechanical anisotropy. Specifically, the P-[111] showed the highest mechanical response while the P-[100] exhibited the lowest (Figure 9b). Their snapshots records of the compression process and the corresponding FE simulations showed layer-by-layer deformation mechanisms consistent with previous findings (Figure S1–S3, Supporting Information).<sup>[7b,e]</sup>

To compare the mechanical properties of all structures, the mean values of peak stress and Young's modulus were calculated over three tests using the stress–strain curve data, as shown in Figure 10 and Figure S4, Supporting Information. The structures were categorized based on their deformation characteristics, tetragonal (tD, tP) and rhombohedral (H, rPD). These were compared to the baseline G, D, and P structures under equivalent loading conditions and compared them with the G, D, and P structures in corresponding loading directions. As shown in Figure 10a, for tetragonal deformation structures of D, the strongest tD-tDelta-L exhibited 26.5% higher peak stress than D-[100], and tD-tG-T was 9.2% stronger than D-[100]. In the case of tetragonal deformation of P, the peak stress of the strongest tP-oPa-L exceeded P-[100] by 41% and tP-Max-T exceeded P-[100] by 19.4%. These results highlight that bifurcating structures exhibit enhanced compressive mechanical properties. The comparison of rhombohedral deformation structures (Figure 10b) also supports this conclusion. The rhombohedral deformed H generally overperformed G, D, and P structures in most orientations, except for H-max-T. For the rhombohedral deformation from

P to D, rPD-rGL-L and rPD-rGL-F showed 3.8% and 1.7% higher peak stress than the strongest baseline P-[111]. A similar trend was observed for the Young's modulus (Figure 10c,d). The specific energy absorption (SEA) of the samples is shown in Figure S5, Supporting Information.

To compare with other categories of lattices,<sup>[21]</sup> Ashby chart has been added to benchmark our bifurcating TPMS structures (Figure 11). The bifurcating TPMS structures demonstrate exceptional performance due to its outstanding mechanical properties. Despite their relatively low density, these structures exhibit high yield stress and Young's modulus compared to other structures, which indicate an impressive strength-to-weight ratio and stiffness. These results highlight the advantages of bifurcating TPMS designs in terms of both modulus and strength.

In order to better understand their mechanical behaviors, the scanning electron microscopy (SEM) investigations of typical H-Max structures were carried out before and after compression tests as shown in Figure S6, Supporting Information. The samples were loaded to reach 25% strain. Under SEM observation, it can be observed that the sample layers are uniformly arranged and closely connected before compression. During testing, the curved structure of the sample undergoes significant bending, with interlayer tearing occurring at the location where bending is most pronounced. This suggests that, under conditions of extreme deformation, interlayer strength remains a critical factor influencing their mechanical properties. However, we can still effectively analyze its mechanical properties by examining the macroscopic deformation and stress distribution.

Therefore, we calculated and quantified how these stress distributions contribute to enhanced mechanical strength by extracting the volumes of different stress intervals in the simulation. Considering that structures typically reach peak stress at 5% strain, which may result in significant material yielding, the volume proportions in all the structures were extracted at 4% strain and categorized into seven stress intervals: [0, 10 MPa], (10 MPa, 20 MPa], (20 MPa, 30 MPa], (30 MPa, 40 MPa], (40 MPa, 50 MPa], (50 MPa, 60 MPa], and (60 MPa, 67 MPa]. For comparison, the conventional cubic TPMS structures from [21] directions were also calculated. These results are summarized in Table S1, Supporting Information. It can be observed that tD-tDelta-L has a higher proportion of volume in the high stress range compared to other structures, resulting in the highest

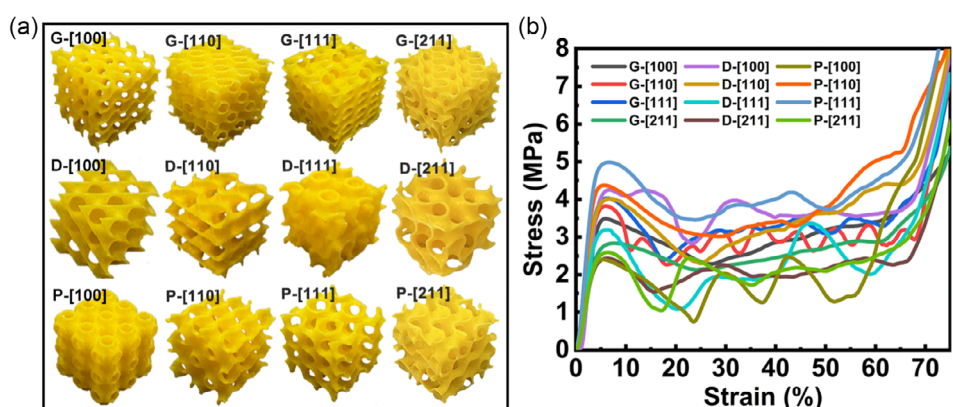
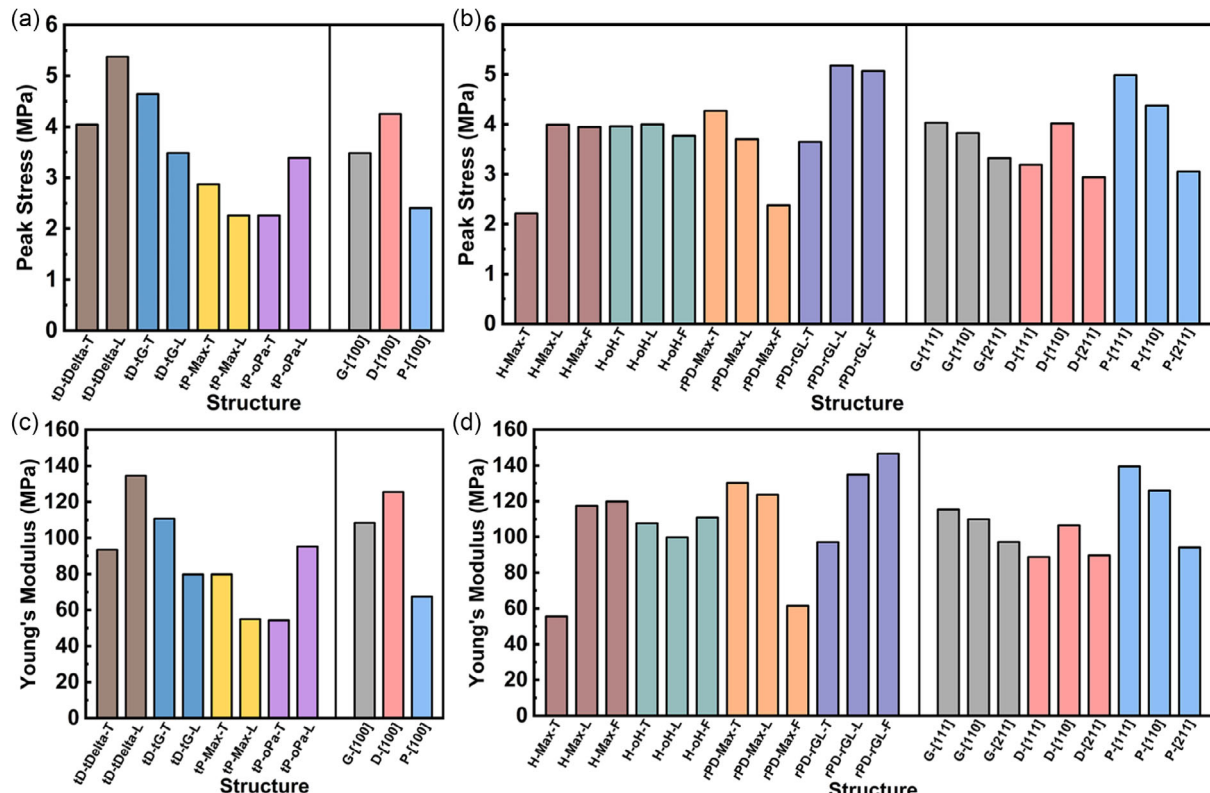


Figure 9. a) 3D-printed G, D, and P structures in different directions. b) Stress–strain curves of G, D, and P structures.



**Figure 10.** Peak stress and Young's modulus of all TPMS structures investigated in this study. The structures were categorized based on their deformation characteristics: a,c) tetragonal (tD, tP) and b,d) rhombohedral (H, rPD).

structural strength. Most of the materials in tP-oPa-T are at low stress levels, resulting in the lowest structural strength. A more intuitive calculation can be performed using the following formula

$$\mu_{\text{distribution}} = \sum_{i=1}^N V_i \bar{\sigma}_i \quad (2)$$

where  $\mu_{\text{distribution}}$  is the evaluation indicator for stress distribution,  $\bar{\sigma}_i$  is the average stress in the stress interval, for example, the average stress in the [20 MPa, 30 MPa] stress interval is 25, and  $V_i$  is the volume fraction of the stress interval. The  $\mu_{\text{distribution}}$  of the above structures are shown in Table S2, Supporting Information. The proposed evaluation indicator for stress distribution shows a good correlation with corresponding peak stress of the same structure, which can reflect the relationship between stress distribution and strength. In fact, the increase in peak stress is a macroscale reflection of the improvement in stress distribution, and the comparison of peak stress can reflect the comparison of stress distributions. However, due to the inherent limitations in simulation step sizes across different structures, it is challenging to accurately capture the strain corresponding to the peak stress but can only approach it as closely as possible. On the other hand, the peak stress was obtained through experiments, while the stress distribution index was obtained through simulation. There will also be certain differences between experimental and simulation results. Despite these differences, these

results yield valuable insights into the mechanical behavior of these bifurcating structures.

From the structural point of view, the mechanical properties were closely affected by the geometry of these surfaces. In view of the mathematical gluing constructions,<sup>[22]</sup> it is convenient to simplify the TPMSs as composed of simpler minimal surfaces such as catenoids and helicoids. The vertical straight lines in tD-tDelta, tD-tG, and rPD-rGL surfaces can be seen as the axis of helicoids. When the minimal surface deforms along the classical family (tD or rPD), the axes of helicoids remain straight. But when the minimal surface deforms along the bifurcating family (tDelta, tG or rGL), the axes become helical. On the other hand, the H-Max, rPD-Max, and tP-Max surfaces can be seen as consisting of catenoids. When the lattice deforms along the symmetry axis of the catenoids, the waist of the catenoids may expand or shrink. The H-oH and tP-oPa surfaces also consist of catenoids, but bifurcation occurs when the surface deforms along a direction perpendicular to the axes of catenoids. The surface deforms along the classical family (H or tP), the positions of the catenoids remain symmetric; when the surface deforms along the bifurcating family (oH or oPa), the catenoids shift away from symmetric positions.

A classical nonbifurcating TPMS, usually, does not remain as minimal surface under the mechanical strain. For instance, when the P surface is compressed along the [100] direction, the waist of the catenoids needs to expand for the surface to remain minimal, but they shrink instead under mechanical pressure. For another

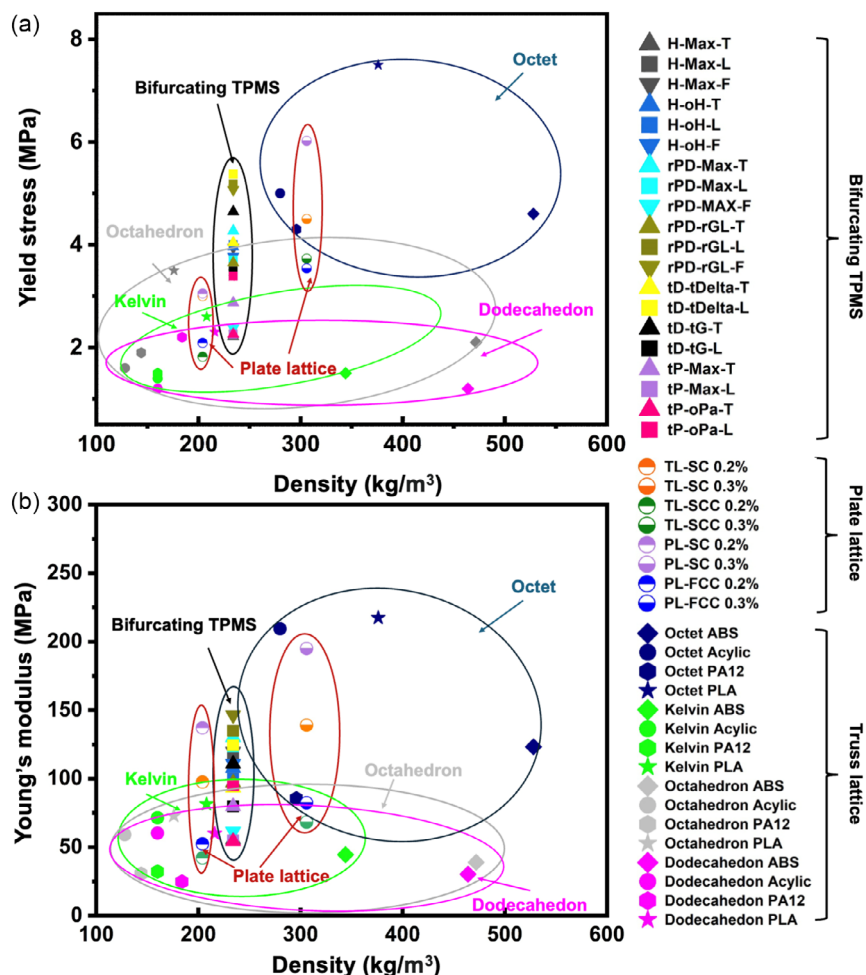


**Figure 11.** Comparison between bifurcating TPMSs and other polymer-based metamaterials<sup>[21]</sup> under compression testing. a) Yield stress and b) Young's modulus versus materials density.

instance, when the D surface is compressed along the [100] direction, the vertical straight lines need to remain straight for the surface to remain minimal, but they would eventually break under mechanical pressure. Notably, conventional TPMS structures exhibit distinct anisotropic mechanical behaviors in various directions following structural modifications or deformation.<sup>[23]</sup> The bifurcating TPMSs are special in that they accommodate an unusual deformation that keeps the surface minimal. As we have shown in the manuscript, this bifurcating phenomenon significantly influences their mechanical properties by altering their symmetry and introducing mechanical anisotropy. Mathematics tells us that bifurcations only occur at nonsymmetric (noncubic) deformations of classical surfaces (tD, tP, H, rPD). Moreover, the new bifurcating branches are less symmetric than the classical branches. Hence at a bifurcating surface, a deformation in the direction that favors bifurcation brings uncertainty: certain symmetries may or may not break. Deformation in other directions, however, would guarantee to break or preserve the symmetries. For instance, when the tP-Max surface is compressed along the T direction, the waist of the catenoids will shrink but the surface remains minimal. Similarly, when the tD-tDelta or tD-tG surface

is compressed along the T direction, the vertical straight lines can bend into helical and the surface remains minimal. Such bending is the opposite for neighboring helicoids, causing stresses in the structure. Thanks to the unique geometry, the bifurcating TPMSs are more flexible and endure more pressure, which may explain why they exhibit excellent mechanical properties.

The pattern of shear bands is also closely related to the geometry. Helicoidal structures (e.g., tD-tDelta-T and tD-tG-T) break at horizontal lines because these are the weakest connections. Catenoidal structures (e.g., H-Max-F, rPD-Max-T, tP-Max-L, and tP-oPa-T.) tend to break at their waist, forming horizontal shearing bands. However, there are also oblique shearing bands that appeared, as seen in tP-Max-T and tP-oPa-L. This can be explained by the anisotropy. The cubic P surface can be seen as composed of catenoids with axes in either vertical or horizontal. After a vertical deformation, the horizontal catenoids tilt, so the symmetry breaks.

In addition, when the structural forms are the same (helicoids or catenoids), the variation in the height of helicoids or catenoids also plays an important effect on the structural mechanical properties. For example, tD-tDelta and tD-tG showed different

number of repeating units under the same boundary condition due to the different heights of the helicoids. The findings reveal that the greater the number of repeating units along the loading direction, the more favorable it is for the structure to maintain its strength under compressive loads. Compared with the tD-tG-T structure, the tD-tDelta-L structure, with the same number of repeating units in the load direction but more repeating units in the horizontal direction, exhibited a more uniform stress distribution and achieved the highest compressive stress.

This phenomenon is also reflected in structures composed of catenoids, such as tP-Max and tP-oPa. Due to the different heights of the catenoids surfaces, the orientation of the long axes of the elliptical pores in the structures is distinct. The tP-Max-L and tP-oPa-T structures, characterized by their flat elliptical pores, are prone to local deformation dominated by bending, thereby facilitating the collapse of layers and exhibiting lower mechanical strength. Conversely, the elliptical pores in the tP-Max-T and tP-oPa-L structures are vertical, which promotes local deformation mainly caused by stretching, thus resulting in stronger mechanical properties.

It is also worth noting that the bifurcating TPMSs are special in that they accommodate an unusual deformation that keeps the surface minimal. As we have shown in the manuscript, this bifurcating phenomenon significantly influences their mechanical properties by altering their symmetry and introducing mechanical anisotropy. Mathematics tells us that bifurcations only occur at nonsymmetric (noncubic) deformations of classical surfaces (tD, tP, H, rPD). Moreover, the new bifurcating branches are less symmetric than the classical branches. Hence at a bifurcating surface, a deformation in the direction that favors bifurcation brings uncertainty: certain symmetries may or may not break. Deformation in other directions, however, would guarantee to break or preserve the symmetries. This leads to the significant mechanical anisotropy that we observed here. However, it is still challenging to fully explain their anisotropic response at the current stage. Further studies are under way.

### 3. Conclusions

In this article, eight bifurcating TPMS structures were designed and fabricated. Considering the anisotropy of these structures, 3D printing and compression tests were carried out from multiple directions. The peak stress and Young's modulus of these samples were obtained from the experimental stress-strain curves and compared to those of the commonly studied G, D, and P structures. Our results demonstrated that the bifurcating TPMS structures showed higher strength under compressive loads compared to classical counterparts. Specifically, tetragonal deformation structure tD-tDelta-L showed a 26.5% increase in peak stress over D-[100], while tP-oPa-L exhibited a 41% improvement relative to P-[100]. Furthermore, the rhombohedral deformation structure rPD-rGL-L achieved a 3.8% higher peak stress than the strongest structure P-[111]. In general, the investigation of bifurcations expands the mechanical potential of TPMS structures. Their mechanical characteristics not only ensures the durability of the material under load but also makes it highly versatile for various applications where lightweight yet robust

materials are required. Besides, the deformation of the underlying lattice opens up new opportunities for adjusting the structural geometry to achieve enhanced mechanical performance. This advancement is crucial for advancing lightweight and multifunctional applications of TPMS structures, offering new possibilities for material design and optimization.

### 4. Experimental Section

**Scaffold Design and Manufacturing:** The generation of the bifurcating TPMS structural units is detailed in Results and Discussion. The structural units of eight bifurcating TPMSs were obtained using Surface Evolver, which were then imported into the 3D modeling software Houdini to get the periodic lattices, and then Boolean operations were performed with a cube to obtain the target structure model. All samples were fabricated using an FDM 3D printer (Raise 3D Pro2) with PLA filament with a diameter of 1.75 mm obtained from Polymaker components, and the main printing parameters are given as follows: layer thickness of 0.15 mm, printing speed of  $40 \text{ mm s}^{-1}$ , nozzle diameter of 0.3 mm, printing temperature of  $205^\circ\text{C}$ , and build plate temperature of  $60^\circ\text{C}$ . The size of all printed models was  $40 \times 40 \times 40 \text{ mm}$ .

**Mechanical Compression Test:** All scaffolds were subjected to a uniaxial quasistatic compression test using an FR-103C testing machine with 50 KN load cell at a strain rate of  $1 \text{ mm min}^{-1}$  at room temperature to evaluate the compression performance. The loading direction was consistent with the printing direction of all scaffolds, and the test was terminated after densification. Stress-strain curves were accordingly extracted by dividing the recorded forces by the nominal cross-section area ( $40 \times 40 \text{ mm}^2$ ) to get stress and dividing the change in the length along the compressing direction by the initial length (40 mm) to obtain strain. The engineering strain/stress was used in all the figures. Elastic modulus and compressive strength were calculated according to the slope of the first linear region in stress-strain curves and the highest recorded stress, respectively. Images of the front view of these models were taken during the compression process to record the deformation processes. The mechanical properties of the base material were obtained from the uniaxial compressive test on a PLA cylinder sample with a size of  $\Phi 12.7 \times 25.4 \text{ mm}$  and a loading speed of  $1 \text{ mm min}^{-1}$  according to ASTM D695, giving an elastic modulus of 1400 MPa and yield stress of 57 MPa.

**Simulation Procedure:** For FE simulation, the models were meshed using FE meshing software Ntopology with element type C3D4 and then imported into Abaqus 6.14 for FE calculation. The type of analysis performed was explicit, dynamic. The mechanical properties of the materials used in the simulation were measured experimentally, with an elastic modulus of 1400 MPa, a Poisson's ratio of 0.3, and a yield strength of 57 MPa, and the strain hardening phenomenon was considered. The specific parameters of strain hardening were automatically generated by importing the curves obtained from compression experiments into the "calibrations" module in Abaqus 6.14. In the simulation of each structure, the upper and lower end faces were constrained by rigid bodies to simulate the action of the compression plate in the experiment. The contact was considered between the rigid body and the structure as well as the structure itself. Therefore, we imposed the general contact on the simulation model. In the contact property, the tangential behavior adopts a penalty friction formulation with a friction coefficient of 0.3, and the normal behavior is defined as hard contact. In all simulations, fix the lower rigid body and impose displacement boundary conditions on the upper rigid body to be consistent with the actual situation of the compression experiments. The deformation, contact force, and Von Mises stress contours of all structures are exported as simulation results. The reliability of the simulation results is determined by comparing the stress-strain curves obtained from both simulations and experiments. Subsequently, the deformation mechanism of the structure is analyzed based on the simulated stress contours.

## Supporting Information

Supporting Information is available from the Wiley Online Library or from the author.

## Acknowledgements

This work was supported by the National Natural Science Foundation of China (grant nos. 22373074 and 12002238), National Key Research and Development Program of China (grant no. 2022YFC2403200), and Fundamental Research Funds for the Central Universities, the Program for Professor of Special Appointment (Eastern Scholar) at Shanghai Institutions of Higher Learning and the Shanghai Pujiang Program (2020PJD072).

## Conflict of Interest

The authors declare no conflict of interest.

## Author Contributions

**Yanhong Zhang:** formal analysis (equal); investigation (lead); methodology (equal); software (lead); visualization (lead); writing—original draft (lead). **Junming Zhang:** formal analysis (equal); software (equal); validation (equal); writing—review & editing (supporting). **Xiaotian Chen:** investigation (supporting); visualization (supporting); writing—review & editing (supporting). **Weidong Yang:** funding acquisition (supporting); project administration (supporting); writing—review & editing (supporting). **Hao Chen:** conceptualization (equal); formal analysis (equal); funding acquisition (supporting); investigation (supporting); project administration (supporting); supervision (supporting); writing—review & editing (supporting). **Shunai Che:** investigation (supporting); supervision (supporting); writing—review & editing (supporting). **Lu Han:** conceptualization (lead); formal analysis (equal); funding acquisition (lead); investigation (equal); project administration (lead); supervision (lead); writing—review & editing (lead). **Yanhong Zhang** and **Junming Zhang** contributed equally to this work.

## Data Availability Statement

The data that support the findings of this study are available from the corresponding author upon reasonable request.

## Keywords

3D printing, bifurcating, mechanical properties, stress distributions, triply periodic minimal surfaces

Received: October 28, 2024

Revised: February 23, 2025

Published online:

- [1] a) S. Hyde, S. Andersson, K. Larsson, T. Landh, Z. Blum, S. Lidin, B. W. Ninham, in *The Language of Shape*, Elsevier Science B.V., Amsterdam, The Netherlands. **1997**; b) S. Andersson, S. T. Hyde, K. Larsson, S. Lidin, *Chem. Rev.* **1988**, *88*, 221.
- [2] a) L. Han, S. Che, *Adv. Mater.* **2018**, *30*, e1705708; b) L. Xiang, Q. Li, C. Li, Q. Yang, F. Xu, Y. Mai, *Adv. Mater.* **2023**, *35*, 2207684.
- [3] a) T. Fu, X. Hu, C. Yang, *Appl. Math. Model.* **2023**, *124*, 553; b) A. Almesmari, I. Barsoum, R. K. A. Al-Rub, *Virtual Phys. Prototyp.* **2024**, *19*, e2308514; c) A. Bayati, D. Rahmatabadi, I. Chasemi, M. Khodaei, M. Baniassadi, K. Abrinia, M. Baghani, *Mater. Lett.* **2024**, *361*, 136075.

- [4] a) R. Pugliese, S. Graziosi, *Slas Technol.* **2023**, *28*, 165; b) J. Feng, J. Fu, X. Yao, Y. He, *Int. J. Extreme Manuf.* **2022**, *4*, 165; c) O. Al-Ketan, R. K. Abu Al-Rub, *Adv. Eng. Mater.* **2019**, *21*, 1900524; d) S. Torquato, A. Donev, *Proc. R. Soc. A-Math. Phys. Eng. Sci.* **2004**, *460*, 1849.
- [5] a) S. Rajagopalan, R. A. Robb, *Med. Image Anal.* **2006**, *10*, 693; b) D.-J. Yoo, *Int. J. Precis. Eng. Manuf.* **2011**, *12*, 61; c) E. A. Lord, A. L. Mackay, *Curr. Sci.* **2003**, *85*, 346.
- [6] a) M. G. Gado, O. Al-Ketan, M. Aziz, R. A. Al-Rub, S. Ookawara, *Energy Technol.* **2024**, *12*, 2301287; b) J. Feng, J. Fu, X. Yao, Y. He, *Int. J. Extreme Manuf.* **2022**, *4*, 022001; c) A. Almesmari, N. Baghous, C. J. Ejeh, I. Barsoum, R. K. A. Al-Rub, *Polymers* **2023**, *15*, 3858; d) N. Thomas, N. Sreedhar, O. Al-Ketan, R. Rowshan, R. K. Abu Al-Rub, H. Arafat, *Desalination* **2018**, *443*, 256; e) M. Joyce, T. Hodgkinson, M. Lemoine, A. González-Vázquez, D. Kelly, F. O'Brien, *Eur. Cells Mater.* **2023**, *45*, 158; f) N. V. Viet, N. Karathanasopoulos, W. Zaki, *Mech. Mater.* **2022**, *172*, 104363.
- [7] a) N. Wang, G. K. Meenashisundaram, S. Chang, J. Y. H. Fuh, S. T. Dheen, A. Senthil Kumar, *J. Mech. Behav. Biomed. Mater.* **2022**, *129*, 105151; b) L. Zhang, S. Feih, S. Daynes, S. Chang, M. Y. Wang, J. Wei, W. F. Lu, *Addit. Manuf.* **2018**, *23*, 505; c) M. M. Sychov, L. A. Lebedev, S. V. Dyachenko, L. A. Nefedova, *Acta Astronaut.* **2018**, *150*, 81; d) Z. H. Lin, J. H. Pan, H. Y. Li, *Polymers* **2022**, *14*, 2885; e) S. M. Sajadi, P. S. Owuor, S. Schara, C. F. Woellner, V. Rodrigues, R. Vajtai, J. Lou, D. S. Galvão, C. S. Tiwary, P. M. Ajayan, *Adv. Mater.* **2018**, *30*, 1704820.
- [8] a) A. M. Abou-Ali, O. Al-Ketan, R. Rowshan, R. Abu Al-Rub, *J. Mater. Eng. Perform.* **2019**, *28*, 2316; b) Z. Qin, S. Jung Gang, J. Kang Min, J. Buehler Markus, *Sci. Adv.* **2017**, *3*, e1601536; c) F. S. L. Bobbert, K. Lietaert, A. A. Eftekhari, B. Pouran, S. M. Ahmadi, H. Weinans, A. A. Zadpoor, *Acta Biomater.* **2017**, *53*, 572; d) D. W. Abueidda, M. Bakir, R. K. Abu Al-Rub, J. S. Bergström, N. A. Sobh, I. Jasiuk, *Mater. Des.* **2017**, *122*, 255; e) J. Kadkhodapour, H. Montazerian, A. C. Darabi, A. P. Anaraki, S. M. Ahmadi, A. A. Zadpoor, S. Schmauder, *J. Mech. Behav. Biomed. Mater.* **2015**, *50*, 180; f) S. M. Ahmadi, S. A. Yavari, R. Wauthle, B. Pouran, J. Schroeten, H. Weinans, A. A. Zadpoor, *Materials* **2015**, *8*, 1871; g) C. Yan, L. Hao, A. Hussein, S. L. Bubb, P. Young, D. Raymont, *J. Mater. Process. Technol.* **2014**, *214*, 856; h) A. Viswanath, K. A. Khan, I. Barsoum, *Mater. Des.* **2022**, *224*, 111293.
- [9] a) A. Singh, N. Karathanasopoulos, *Compos. Sci. Technol.* **2024**, *253*, 110632; b) Z. Luo, Q. Tang, J. Song, Y. Zhang, Q. Feng, S. Ma, R. Setchi, M. Zhao, *Compos. Struct.* **2024**, *349*, 118555.
- [10] a) F. Li, J. Gan, L. Zhang, H. Tan, E. Li, B. Li, *Compos. Sci. Technol.* **2024**, *245*, 110365; b) N. Novak, O. Al-Ketan, M. Borovinšek, L. Krstulović-Opara, R. Rowshan, M. Vesenjak, Z. Ren, *J. Mater. Res. Technol.* **2021**, *15*, 1318.
- [11] a) F. Liu, Z. Mao, P. Zhang, D. Z. Zhang, J. Jiang, Z. Ma, *Mater. Des.* **2018**, *160*, 849; b) O. Al-Ketan, D. W. Lee, R. Rowshan, R. K. Abu Al-Rub, *J. Mech. Behav. Biomed. Mater.* **2020**, *102*, 103520; c) N. Qiu, J. Zhang, F. Yuan, Z. Jin, Y. Zhang, J. Fang, *Eng. Struct.* **2022**, *263*, 114377; d) N. Qiu, J. Zhang, C. Li, Y. Shen, J. Fang, *Int. J. Mech. Sci.* **2023**, *246*, 108118; e) H. Nguyen-Xuan, K. Q. Tran, C. H. Thai, J. Lee, *Compos. Struct.* **2023**, *315*, 116981; f) S. Y. Choy, C.-N. Sun, K. F. Leong, J. Wei, *Mater. Des.* **2017**, *131*, 112; g) C. J. Ejeh, I. Barsoum, A. M. Abou-Ali, R. K. A. Al-Rub, *J. Mater. Res. Technol.* **2023**, *27*, 6076.

- [12] a) X. Y. Li, Z. H. Jin, X. Zhou, K. Lu, *Science* **2020**, *370*, 831; b) I. Maskery, A. O. Aremu, L. Parry, R. D. Wildman, C. J. Tuck, I. A. Ashcroft, *Mater. Des.* **2018**, *155*, 220.
- [13] a) N. Yang, K. Zhou, *Mater. Sci. Eng., C* **2014**, *43*, 502; b) Y. Li, Q. Xia, S. Yoon, C. Lee, B. Lu, J. Kim, *Comput. Phys. Commun.* **2021**, *264*, 107956.
- [14] a) W. Wang, Y. Jin, Y. Mu, M. Zhang, J. Du, *Virtual Phys. Prototyp.* **2023**, *18*, e2203701; b) W. Jiang, W. Liao, T. Liu, X. Shi, C. Wang, J. Qi, Y. Chen, Z. Wang, C. Zhang, *Mater. Des.* **2021**, *204*, 109655; c) H. Jia, H. Lei, P. Wang, J. Meng, C. Li, H. Zhou, X. Zhang, D. Fang, *Extreme Mech. Lett.* **2020**, *37*, 100671; d) H. Yin, Z. Liu, J. Dai, G. Wen, C. Zhang, *Compos. Pt. B-Eng.* **2020**, *182*, 107565; e) Y. Jiang, J. Hu, S. Wang, N. Lei, Z. Luo, L. Liu, *Comput.-Aided Des.* **2023**, *162*, 103554; f) J. Feng, J. Fu, C. Shang, Z. Lin, B. Li, *Comput.-Aided Des.* **2019**, *115*, 307; g) F. Günther, S. Pilz, F. Hirsch, M. Wagner, M. Kästner, A. Gebert, M. Zimmermann, *Addit. Manuf.* **2023**, *73*, 103659; h) X. Chen, M. Hu, Y. Sun, J. Yang, L. Bai, Y. Xiong, *Mater. Des.* **2022**, *224*, 111370; i) Y. Zhang, J. Zhang, X. Zhao, Y. Li, S. Che, W. Yang, L. Han, *Addit. Manuf.* **2022**, *58*, 103036; j) F. Alawwa, I. Barsoum, R. K. A. Al-Rub, *Mech. Adv. Mater. Struct.* **2024**, *31*, 8691.
- [15] H. Chen, *Indiana Univ. Math. J.* **2021**, *70*, 1543.
- [16] a) M. Koiso, P. Piccione, T. Shoda, *Ann. Inst. Fourier* **2018**, *68*, 2743; b) H. Chen, M. Weber, *Trans. Am. Math. Soc.* **2021**, *374*, 2785; c) H. Chen, M. Weber, *Trans. Am. Math. Soc.* **2021**, *374*, 2057.
- [17] A. Fogden, S. T. Hyde, *Acta Crystallogr., Sect.: Found Crystallogr.* **1992**, *48*, 442.
- [18] a) A. Fogden, S. T. Hyde, *Eur. Phys. J. B –Condens. Matter Complex Syst.* **1999**, *7*, 91; b) A. Fogden, M. Haeberlein, S. Lidin, *J. Phys.* **1993**, *3*, 2371.
- [19] a) S. Tabacu, C. Ducu, *Extreme Mech. Lett.* **2020**, *39*, 100775; b) T. J. Coogan, D. O. Kazmer, *J. Rheol.* **2019**, *63*, 655.
- [20] Y. Sun, W. Tian, T. Zhang, P. Chen, M. Li, *Mater. Des.* **2020**, *185*, 108239.
- [21] a) E. Truszkiewicz, A. Thalhamer, M. Rossegger, M. Vetter, G. Meier, E. Rossegger, P. Fuchs, S. Schlögl, M. Berer, *J. Appl. Polym. Sci.* **2021**, *139*, e51618; b) T. Li, F. Jarrar, R. A. Al-Rub, W. Cantwell, *Int. J. Solids Struct.* **2021**, *230*, 111153.
- [22] H. Chen, D. Freese, *Proc. R. Soc. A-Math. Phys. Eng. Sci.* **2022**, *478*, 20220431.
- [23] a) X. Peng, Q. Huang, Y. Zhang, X. Zhang, T. Shen, H. Shu, Z. Jin, *Mater. Des.* **2021**, *205*, 109706; b) S. Altamimi, D.-W. Lee, I. Barsoum, R. Rowshan, I. M. Jasiek, R. K. A. Al-Rub, *Mech. Adv. Mater. Struct.* **2025**, *32*, 79; c) P. J. L. Lazar, J. Subramanian, E. Natarajan, K. Markandan, S. Ramesh, *J. Mater. Res. Technol.* **2023**, *24*, 9562; d) H. Jiang, B. A. Bednarcyk, L. L. Barbenchon, Y. Chen, *Thin-Walled Struct.* **2023**, *192*, 111115; e) N. Yang, Z. Qian, H. Wei, M. Zhao, *Mater. Des.* **2023**, *225*, 111595.
- [24] H. Chen, M. Traizet, *J. Reine Angew. Math.* **2024**, *808*, 1.